



# Towards detection of cancer biomarkers in human exhaled air by transfer-learning-powered analysis of odor-evoked calcium activity in rat olfactory bulb

Mikhail V. Kopeliovich<sup>a</sup>, Mikhail V. Petrushan<sup>a,b</sup>, Aleksey E. Matukhno<sup>b</sup>, Larisa V. Lysenko<sup>b,c,\*</sup>

<sup>a</sup> WizaTech LLC, Rostov-on-Don, 344082, Russia

<sup>b</sup> Research Center for Neurotechnology, Southern Federal University, Rostov-on-Don, 344090, Russia

<sup>c</sup> Department of Physics, Southern Federal University, Rostov-on-Don, 344090, Russia

## ARTICLE INFO

### Keywords:

Gastric cancer  
Breath analysis  
Biomarker  
Calcium imaging  
Pre-training model  
Synthetic data generation

## ABSTRACT

Detection of volatile organic compounds in exhaled air is a promising approach to non-invasive and scalable gastric cancer screening. This work proposes a new approach for the detection of volatile organic compounds by analyzing odor-evoked calcium responses in the rat olfactory bulb. We estimate the feasibility of gastric cancer biomarker detection added to the exhaled air of healthy participants. Our detector consists of a convolutional encoder and a similarity-based classifier over encoder outputs. To minimize overfitting on a small available training set, we involve a pre-training where the encoder is trained on synthetic data representing spatiotemporal patterns similar to real calcium responses in the olfactory bulb. We estimate the classification accuracy of exhaled air samples by matching their encodings with encodings of calibration samples of two classes: 1) exhaled air and 2) a mixture of exhaled air with the cancer biomarker. On our data, the accuracy increased from 0.68 on real data up to 0.74 if pre-training on synthetic data is involved. Our work is focused on proving the feasibility of proposed new approach rather than on comparing its efficiency with existing methods. Such detection is often performed with an electronic nose, but its output becomes unstable over time due to a sensor drift. In contrast to the electronic nose, rats can robustly detect low concentrations of biomarkers over lifetime. The feasibility of gastric cancer biomarker detection in exhaled air by bio-hybrid system is shown. Pre-training of neural models for images analysis increases the accuracy of detection.

## 1. Introduction

Early detection of cancer is a key factor to efficient treatment and prolongation of a patient's lifetime. Gastric cancer (GC) remains the third leading cause of death from cancer worldwide [1,2]. Unspecific clinical symptoms with many other benign gastrointestinal disorders often delay the diagnosis of GC, leading to extremely poor prognosis. Earlier diagnosis substantially improves the prognosis: 95% of patients with cancer that is confined to the inner lining of the stomach wall will survive longer than 5 years [3]. Therefore, early detection of GC is extremely important and should be noninvasive, cheap, convenient, and quick in diagnosis.

\* Corresponding author. Research Center for Neurotechnology, Southern Federal University, Rostov-on-Don, 344090, Russia.  
E-mail address: [lalv@yandex.ru](mailto:lalv@yandex.ru) (L.V. Lysenko).

<https://doi.org/10.1016/j.heliyon.2023.e20173>

Received 19 January 2023; Received in revised form 4 September 2023; Accepted 13 September 2023

Available online 17 September 2023

2405-8440/© 2023 Published by Elsevier Ltd.

This is an open access article under the CC BY-NC-ND license

(<http://creativecommons.org/licenses/by-nc-nd/4.0/>).

## Abbreviations

3D	Three-dimensional space
FN	False negative
FP	False positive
GC	Gastric cancer
kNN	k-nearest neighbors algorithm
TN	True negative
TP	True positive
VOC	Volatile organic compound

Certain volatile organic compounds (VOCs) can serve as biomarkers of GC. Noninvasive screening method for digestive cancer can be based on detecting such VOCs in exhaled breath of patients [4–7]. This is because the volatile compounds (or their pattern) in cancer cells differ from those in healthy tissues. Exhaled air of cancer patients contains several hundreds of compounds. Predominant part of these compounds is also presented in the exhalation of healthy people. Therefore, it is important to determine the substance which is a marker of cancer and to detect it in a feasible range of concentrations. According to the patent # RU2538625C1 [8] such a non-selective marker is cyclohexyl isothiocyanate, presented in the air exhaled by patients with the cancer of lungs, stomach, skin, bladder, mammary gland, but not found in the breath of people who do not have malignant tumors. Among the main biomarkers, considered relevant to GC diagnosis, is listed 6-methyl-5-hepten-2-one [9,10]. Chemical analysis found that 6-methyl-5-hepten-2-one was significantly elevated in patients with GC as compared with less severe gastric conditions in two genetically different populations of patients with different eating habits and geographical location [11].

Currently, artificial olfactory systems, electronic nose devices, which include a set of sensors associated with signal processing tools, have gained wide popularity [12–14]. E-noses have a high diagnostic accuracy for the detection of cancer in exhaled breath, but they display a high heterogeneity in the sensitivity, ranged from 48.3% to 95.8% and the specificity from 10.0% to 100.0% [15]. They require calibration, and their results are often unstable [12,16]. It is assumed that the inclusion of sensitive components of biological olfactory systems into gas-sensitive materials can increase selectivity for VOCs of the obtained gas sensors and bioelectronic systems [17–19]. Difficulties in introducing biomaterials into the design of biosensors are associated with individuality of biological systems behavior and dependency of the behavior on general functional state of an animal. Another way to use a biological nose is to employ trained animals. The sense of smell of trained dogs has been successfully used for cancer detection [20–23]. However, dogs require expensive care and training/retraining costs and are highly susceptible to external interference. At the same time, a bio-electronic nose based on rodent brain-machine interface and machine learning techniques has a comparable sensitivity to the trained animal and can detect odors on a variable background [24,25].

The presence of many olfactory receptors in the olfactory epithelium of the nose of animals provides high sensitivity to a wide range of different chemicals. Such a simultaneous latitude and sensitivity are almost impossible to achieve with artificial sensors [26]. Glomerular layer, where responses from a few thousands olfactory receptor neurons are combined and transmitted via olfactory bulb output neurons to high brain areas is the first area that processes olfactory information. Differences in the spatial activation patterns of glomeruli are thought to play a primary role in identifying odors [27–32].

The traditional procedure of data classification includes preprocessing, feature extraction, and development of a classification model. Similar operations are applicable to the visual data of the charm bulb [33]. Fourier transform, wavelet transforms, and radial basis functions are applied to compute spatial and temporal features, while processing the resulting data with statistical analysis techniques such as Principal component analysis, Support vector machine, k-nearest neighbors (kNN), and Artificial Neural Networks [33,34]. The features in a video image are complicated, so it appears to be a more efficient approach to combine feature extraction and classification procedures into one model, a deep artificial neural network, particularly Convolutional Neural Network [34].

In the present study, we consider a new approach to the analysis of exhaled air by a “bio-hybrid” system involving a) a biological component: anesthetized freely breathing rat with implanted cranial window and b) a technical subsystem for retrieving, processing and analyzing glomerular activity. Using calcium imaging we intercept the olfactory information at the level of glomeruli, where the signals from multiple olfactory receptor neurons are integrated. A cancer biomarker in human exhaled air being smelled by rats expects to cause a specific pattern of glomerular activation in the olfactory bulb. These patterns are represented in a form of calcium dynamics recorded by two-photon microscope as images sequence. Further, specific activation patterns can be recognized by computer vision algorithms to make conclusions about smelled substances.

We consider presented work as a feasibility study towards such a new approach where we aim to prove feasibility of recognizing cancer biomarkers in exhaled air by analyzing calcium response in the rat olfactory bulb on a short series of experiments. Since odor-specific glomerular patterns vary among different species and depend on the concentration of a smelled substance, we reduced the effect of individuality and concentration by the following approach. A GC biomarker of known concentration was added to exhaled air of a healthy participant. Then, taking olfactory responses on exhaled air from one particular person and exhaled air + biomarker (exhaled air of the same person with the added cancer biomarker) as references of two classes, we want to distinguish between the olfactory responses of the same animal on another series of exhaled air and exhaled air + biomarker collected from another participant. The first series of exhaled air and exhaled air + biomarker can be treated as calibration series. The second - as evaluation series. By conducting feasibility experiment, we aim to evaluate similarity of correspondent glomerular responses on evaluation series to

responses on calibration series. It is expected that exhaled air + biomarker-evoked response doesn't depend strongly on exhaled air itself, but mainly on additional cancer biomarker. Particularly, we aim to verify if such similarity of responses on exhaled air + biomarker preserves when calibration and evaluation of exhaled air are collected from different participants.

To formalize a similarity between glomerular responses we search for transform from series of calcium dynamics images to a compact vector (encoding) - the transform, which minimizes a distance between encodings of the same class (exhaled air class or exhaled air + biomarker class) and simultaneously maximizes a distance between encodings of different classes. Such a problem definition is typical for siamese neural networks [35] trained with triplet loss function. Taking into account our small experimental data collected within this feasibility study, we can expect overfitting of a model or low accuracy of classification. Therefore, we involve pre-training phase where we train our model on synthetic data. We don't aim to produce mathematically precise model of odor-evoked calcium dynamics and its representation in calcium images. Instead, we created a mathematical model which produces spatiotemporal pattern based on empirically observed qualities inherent to real calcium imaging data. We expect that training neural model on such synthetic data enhances its capability to operate in spatiotemporal domain relevant to real data.

## 2. Data

The dataset contains real and synthetic data. Real data is generated by laser scanning microscopy of the calcium response in the rat olfactory bulb glomeruli to odor inhaled by the rat. Synthetic data is generated to mimic patterns occurring in the real data.

### 2.1. Real data

#### 2.1.1. Animals

Experiments were performed on 4 adult (aged 7–10 months, weight 350–470 g) male Norway rats (*Rattus norvegicus*) obtained from the Institute of Cytology and Genetics (Novosibirsk, Russia). The rats were kept under 12/12-h light/dark cycle in individual cages at constant temperature ( $23 \pm 1$  °C) and humidity. Food (Complete extruded combo feed for laboratory animals, JSC Gatchinskiy compound feed plant) and purified water were available ad libitum. All experimental procedures were approved (Protocol No 4, Date of approval April 28, 2022) in advance by the Ethics Committee of Southern Federal University (Rostov-on-Don, Russia).

#### 2.1.2. Sample collection

The study protocol was approved by the Ethics Committee of Southern Federal University (Protocol No 1, Date of approval May 11, 2018). All participants provided written, informed consent before inclusion. The study involved 8 healthy nonsmoking volunteers. Inclusion criteria were the absence of acute illness within two weeks prior to sample collection and the absence of chronic bronchopulmonary, cardiovascular, digestive, urinary and reproductive pathologies. Humans with periodontitis were excluded. Other exclusion criteria included any general health issues, such as diabetes, kidney disease, gastric or heart disease, as well as smoking. The average age of the volunteers was  $44 \pm 6$  years. The procedure of exhaled air sampling was as follows. Samples were taken before or 2 h after eating. Volunteers were not allowed to drink anything except water 2 h before the experiment. The air was collected into 10 L sampling bags made of Tedlar material (NikiMLT LLC, Russia). From two to four samples of exhaled air were collected from each volunteer: one control sample and the others with biomarkers added. 6-methyl-5-hepten-2-one 99% (ng/ml, CAS Number:110-93-0, Sigma-Aldrich, USA) was used as a biomarker of stomach cancer. Cyclohexyl isothiocyanate 98% (ng/ml, CAS Number:1122-82-3, Sigma-Aldrich, USA) was used as a nonspecific biomarker regardless of cancer location [8].

The liquid biomarkers were drawn up with a glass micropipette attached to Nanoliter 2020 Injector (WPI Inc., USA) or 1–100  $\mu$ L syringe and injected into the 10 L Tedlar bag. The small puncture hole in the bag was subsequently sealed with tape. The procedure is similar to those described in Ref. [36].

The required liquid volume VOC for a desired concentration can be calculated by using the following equation:

$$V_{voc} = \frac{MV_{mix}C}{\rho V_m},$$

with M representing the VOC's molar mass,  $V_{mix}$  the volume of the Tedlar bag (10 L), c the desired concentration of VOC ( $c = [\text{ppm}] 10^{-6}$ ,  $c = [\text{ppb}] 10^{-9}$ ),  $\rho$  the density of the liquid VOC, and  $V_m$  the molar volume of an ideal gas at room temperature and ambient pressure.

The time between adding the biomarkers to the sample of exhaled air and providing the air to the animal did not exceed 60 min, which ensured the absence of pronounced degradation of the biomarker.

#### 2.1.3. Surgical procedures

Surgical procedures were the same as in Ref. [37]. Since background adaptation and sensitivity to target odors over odorous backgrounds are qualitatively similar in awake and anesthetized animals [38] and experimental conditions in anesthetized rodents are experimentally stable both mechanically and physiologically comparing to awake animals [39], we used anesthetized rats in our study. Rats were anesthetized with a mixture of xylazine hydrochloride 10–15 mg/kg (Xyla, Interchemie, Netherlands) and bases of tiletamine and zolazepam 10 mg/kg (Zoletil, Virbac Lab, Carros, France). The rats received a single i.p. bolus of mannitol (1 g/kg, dissolved in 0.9% w/v NaCl; 2 M; Mannit, Biochemist, Russia) to lower the intracranial pressure. In order to avoid mucosal discharge and nasal blockage the rats were injected with atropine (0.03 mg/kg, intramuscularly). The animals were excluded if anesthesia resulted in

obstruction of the airways and atropine does not help to inhibit the salivary and mucus glands, and if excessive bleeding occurs during durotomy or if bleeding has resulted underneath the center portion of the cranial window, preventing the collection of imaging data. The core temperature was maintained by a heated blanket at  $\sim 37^\circ\text{C}$  and measured by a rectal probe. Once anesthetized, the rats were placed in a stereotaxic apparatus (SR-10AR, NARISHIGE, Japan), and the bone and dura mater overlying the dorsal surface of the left olfactory bulb ( $\sim 3$  mm anteroposterior  $\times$  2 mm mediolateral) was removed under visual control with a stereomicroscope Leica M50 (Leica, Germany). Then the olfactory bulb was bolus loaded with calcium-sensitive dye Cal-590 AM, 1 mM (AAT Bioquest, USA). The methodological procedures in our work related to dye loading and visualization of calcium activity using two-photon imaging are consistent with the works of C.H. Tischbirek et al. [40,41]. In particular, the time for uniform staining of brain tissues (the glomerular layer of the OB at a depth of 100–400  $\mu\text{m}$  from the surface) after a bolus loading of the dye before laser scanning was 1 h or more. Bolus loading of the dye was carried out at several (3–4) points. This made it possible to stain the entire dorsal region of the OB opened for scanning. In our experiments, the total scanning time of the dorsal surface of the OB was from 30 to 60 min. Our recording time corresponds to  $>30$  min [41] for serial functional mapping of all pyramidal layers of the mouse primary auditory cortex at single-neuron resolution. Thus, we suppose that total time of calcium activity recording in OB using Cal-590 AM did not affect the quality of data for the implementation of functional mapping. The cranial window was filled with 1.5% agarose gel (Merck, Germany) and a trepanation hole was closed using the 5-mm coverslip 0.17 mm thick (Menzel-Glaser, Gerhard Menzel, Germany) fixed with dental acrylic cement (DentLight-flow, VLADMIVA, Russia). To fix the animal during visualization a head plate (CFR-2, Narishige, Japan) was installed on its head.

#### 2.1.4. Odor stimulation

Control samples of exhaled air and target samples with added biomarkers were delivered orthonasally through a custom-built olfactometer with TTL-controlled solenoid valves (Burkert, Germany), synchronized with the Zeiss LSM 880 (Carl Zeiss, Germany) acquisition computer. The output flow (maintained at 900 mL/min) was connected to a Teflon tube (ID: 4 mm) and connected to a nose mask on the rat lying under Zeiss LSM 880 (Carl Zeiss, Germany). To provide a continuous steady-state environment to the nasal mucosa, we applied humidified and preheated ( $28\text{--}30^\circ\text{C}$ ) air flow between odor stimulations. Odor delivery was precisely time-locked to Zeiss LSM 880 (Carl Zeiss, Germany) acquisition in a block design experiment (40-sec OFF, 5-sec ON, 40-sec OFF) and was controlled through custom made software. Trials using control and target sample were repeated 10 times with a 40 s interstimulus interval to minimize adaptation and habituation.

#### 2.1.5. Imaging

Two-photon  $\text{Ca}^{2+}$  imaging was performed with laser scanning microscope LSM 880 (Carl Zeiss, Germany) equipped with  $10\times$  objective (W Plan-Apochromat  $10\times/0.5$  DIC D-0.17 VIS-IR M27 75 mm). The dorsal olfactory bulb was illuminated with Ti:Sa femtosecond laser (Chameleon Discovery, Coherent, USA) at the wavelength 1040 nm to provide two-photon excitation of calcium-sensitive indicator Cal-590 AM (AAT Bioquest, USA) in glomerular layer. Emission light was collected in the range of 575–610 nm. The laser power was regulated to minimize photobleaching of the indicator. To determine the global spatial organization of glomerular activation over opened OB dorsal surface, the trepanned zone was divided into two sequentially scanned areas, using a zoom factor of 0.7. Scanning was started from the anterior to the posterior part of the left OB. The animal was moved under the microscope with a motorized stage ZDeck HZ101PM (Prior Scientific, UK). The stage controls are integrated into the scanning control software (Zen Black 2.3). The boundaries of the scanning areas were chosen with 10% overlap to stabilize the images without taking into account the boundary of 5 pixels on each side of the area. Image sequences of 490 s duration were acquired at 4.2057 fps temporal resolution and  $256 \times 256$  pixel spatial resolution, with each pixel corresponding to  $4.74 \times 4.74 \mu\text{m}$  of a projected glomerular layer. Data acquisition was controlled by Zen Black 2.3 (Zeiss, Germany).

#### 2.1.6. Image pre-processing

A sequence of tiff images was recorded by a laser scanning microscope as a result of each experiment. Resolution of each image is  $256 \times 256$  pixels. The experiment covers 10 iterations of odor stimulation, which takes 490 s. Each sequence was transformed to a tensor of size  $16 \times 246 \times 246$  by the following procedure.

1. The sequence is split into 10 fragments of a single stimulation trial.
2. For each fragment:
  - a. Motion compensation is performed by computing an average calcium activity image and by aligning each frame to the position of the best correspondence to the average image. The best correspondence is formalized as minimal Euclidean distance between the average image and the aligned frame. The size of each frame is reduced from  $256 \times 256$  pixels to  $246 \times 246$  pixels to avoid edges uncertainty when aligning.
  - b. Computing the background by averaging frames over 15 s prior to stimulus.
  - c. Computing of relative activity in each frame in a stimulus interval (5 s):

$$\text{relAct}(t, x, y) = \frac{\text{Activity}(t, x, y) - \text{Background}(t, x, y)}{\text{Background}(t, x, y) + \text{Bias}},$$

where:

*Activity* is spatiotemporal distribution of calcium activity in the stimulus interval

*Background* is the average activity in the interstimulus interval (see 2.a).

*Bias* is a positive constant which decreases high relative activity caused by near-zero background. This constant was set to 1 in order to limit possible range of relative activity to [0, 255] – the same range as for activity and background.

3. The resulting sequence of frames (for each stimulation trial) of  $246 \times 246$  pixels is merged into a tensor of size  $16 \times 246 \times 246$ . 16 frames correspond approximately to 3.8 s within the stimulation period.

Resulting tensor represents the spatiotemporal response to a stimulus. We assume that this tensor contains enough specific information to make possible distinguishing between response to clear exhale and response to cancer biomarkers.

Each experiment involves calcium imaging of 2 adjacent areas on the olfactory bulb of a rat, 10 stimulation trials for each area. Thus, in the experiment, we obtain 10 samples per each scanned area. To obtain a concatenated glomerular map, each of 10 samples of the first imaged area can be stitched by spatial dimensions with each of 10 samples of the second scanned area, such giving 100 stitched samples. Further each stitched sample is rescaled to the size of  $16 \times 246 \times 246$  to keep compatibility with single-area imaging and with synthetic data. This rescaling leads to spatial compression along X axis, which, in our opinion, doesn't affect further classification of these samples dramatically.

## 2.2. Synthetic data

Synthetic samples similar to real ones were generated to enlarge the training set for a detector of cancer biomarkers (classifier between clear exhale and cancer biomarker classes). We didn't aim to develop a precise and realistic model of calcium response. Instead, we developed a phenomenological model which reproduces spatiotemporal dynamics visually similar to real calcium dynamics. Our approach is based on the assumption that such visual similarity is sufficient to enhance classifier's ability to distinguish between two different types of responses.

The dataset generation process is based around the attempt to create a semi-realistic model of bioelectrical dynamics inside the olfactory bulb during neural activity occurring in response to a specific odorant. It is theorized and observed in experimental data that there might be one or multiple clusters of activity with strong response to a single type of odorant. Taking into consideration the fact that the activity rises and attenuates over time, our aim was to develop a method to simulate the olfactory bulb activity in the way it is observed during the experiments.

The spatiotemporal dynamics of calcium responses is described by the following formula:

$$f(t, \bar{x}) = \text{Relu}[F + B + UN(\text{ampl})],$$

where:

$F$  is a model of stimulus-related calcium response formalized as a sum of spatiotemporal activity patterns (components):

$$F = \sum_{g=1}^{Ng} H(t - t_0) * A_g * T_g(t) * SP_g(\bar{x}),$$

where:

$Ng$  is the number of calcium signal components

$g$  is the index of a component of calcium response

$t$  denotes time

$\bar{x} = \{x, y\}$  stands for the spatial coordinates vector

$A_g$  is the amplitude if the  $g$  component of the calcium response

$t_0$  is the response onset time

$T_g(t)$  – temporal dynamics of  $g$ -th component of calcium response formalized as a sum of peak response (multiplication of power and exponential functions) which models main effect of glomerular reaction to a stimulus and decayed fluctuation which models respiration related fluctuation of calcium response:

$$T_g(t) = (t - t_0)^{a_g} * e^{-b_g(t-t_0)} + k_g * e^{-v_g(t-t_0)} * \sin(w_g(t - t_0)),$$

where:

$a_g$  is the response growth power

$b_g$  is the response decay power

$k_g$  is the amplitude of the periodic modulation of  $g$ -th response component

$v_g$  is the decay power of the periodic modulation of  $g$ -th response component

$w_g$  is the frequency of the periodic modulation of  $g$ -th response component

$SP_g(\bar{x})$  - spatial distribution of  $g$ -th component of calcium response:

$$SP_g(\bar{x}) = e^{-\frac{(\bar{x} - \bar{m}_g)^T * S_g^{-1} * (\bar{x} - \bar{m}_g)}{2}},$$

where:

$\bar{m}_g$  is the spatial center of  $g$ -th response component

$S_g^{-1}$  is the inverse covariance matrix of spatial distribution of  $g$ -th response component

$H$  – the Heaviside function which sets calcium response to zero for time prior to response onset  $t_0$ .

$B$  is a model of background activity formalized as a sum of  $N_b$  spatiotemporal background patterns (components):

$$B = \sum_{b=1}^{N_b} K_b * \sin(w_b t + \varphi_b) * e^{-\frac{(x-\bar{m}_b)^T S_b^{-1} (x-\bar{m}_b)}{2}}$$

where:

$b$  is the index of background component

$N_b$  is the number of background components

$K_b$  is the amplitude of  $b$ -th background component

$w_b$  is the frequency of  $b$ -th background component

$\varphi_b$  is the phase of  $b$ -th background component

$\bar{m}_b$  is the spatial center of  $b$ -th background component

$S_b^{-1}$  is the inverse covariance matrix of spatial distribution of  $b$ -th background component

$UN(amp)$  is the additive uniform noise sampled from range  $[-amp, +amp]$ .

$Relu$  – Rectified linear unit function:  $Relu(x) = \max(0, x)$ .

The model parameters were chosen manually to obtain samples visually similar to real dynamics. Since the classifier was trained as a Siamese neural network with triplet loss function, three samples are prepared for each train iteration: anchor sample, sample of the same class, and sample of another class. Samples of different classes were generated with different parameters of coordinates of activity centers, amplitude, frequency, growth, decay and other parameters. To generate samples of the same class, coordinates were the same, amplitude and temporal parameters varied in relative range of  $\pm 10\%$ .

### 2.3. Dataset organization

Real and synthetic data form real and synthetic datasets. For the sake of consistency, the data hierarchy in datasets is organized in the same way. A sample will be referred to as a  $16 \times 246 \times 246$  tensor - an elementary item of real or synthetic data, where the first dimension is temporal, the second and the third are spatial. The experiment is a series of samples involving the same rat, volunteer (source of exhaled air), odorant, and its dosage (if the odorant is presented). A group of experiments combines Experiments. For real data, a Group of experiments corresponds to the rat used in the Experiments.

The real dataset involves 4 rats, with 4–7 experiments for each (Table 1). With a rat, two control Experiments (without the cancer biomarker) are performed; other Experiments are performed with the addition of biomarkers (6-methyl-5-hepten-2-one or cyclohexyl isothiocyanate) at different doses.

Two volunteers participated in the experiments. In the control experiments, both volunteers participated; in the experiments with odorants, one or two volunteers could participate, so the values in the cells of the table vary from 0 to 2.

The training part of the Real dataset includes the rats 1, 2 and 3 containing a total of 15 Experiments (1500 samples). The testing part corresponds to the rat 4 with 6 Experiments (600 samples).

Experiments with the cyclohexyl isothiocyanate are included only in the training part of the Real dataset. Since the encoder was trained to distinguish one odorant from another, expanding of the dataset with the additional odorant is expected to facilitate training.

The synthetic dataset doesn't include such categories as a volunteer, odorant, and its dosage. Nevertheless, it is arranged similarly: Groups of experiments contain 2-3 experiments, an experiment combines trials (mostly 20 trials per experiment). Each trial generates a single synthetic sample. A Group of experiments models a real experiment involving a single rat and different odors (one odorant in one experiment). The number of Groups of experiments is 400 for training (23,228 samples) and 25 for validation (1485 samples).

**Table 1**

Summary of biomarker dosages used to collect the Real dataset that includes experiments with rats, stimulated by control samples of exhaled air and target samples with added biomarkers.

Rat	Control experiments	Experiments with 6-Methyl-5-hepten-2-one			Experiments with cyclohexyl isothiocyanate <sup>a</sup>		Total experi-ments
		50 ppb	330 ppm	1650 ppm	18 ppb	18 ppm	
rat 1	2	0	0	2	0	0	4
rat 2	2	0	2	0	0	0	4
rat 3	2	1	0	1	2	1	7
rat 4	2	2	2	0	0	0	6
Total	8	3	4	3	2	1	21

<sup>a</sup> Presented only in the training dataset.

### 3. Methods

The problem of cancer detection in exhaled breath is solved by applying an encoder (to generate sample embeddings) and binary classifier.

The encoder is a convolutional network trained by triplet comparison to generate different embedding vectors for different classes of samples. After training, the encoder parameters are fixed.

Next, the encoder is used to generate sample embeddings for the classifier. The classifier divides the input vectors into two classes based on the reference sample embeddings.

#### 3.1. Encoder architecture

The encoder is a convolutional network based on 3D convolutions (simultaneously by time and space). The encoder input is a sample tensor. The encoder consists of five convolutional blocks, resulting in a tensor of size  $1 \times 4 \times 2 \times 3 \times 3$ , followed by a flatten layer. Thereby the encoder output is a 72-length vector.

Convolutional block contains the following layers: 3D convolution (kernel size is  $3 \times 3 \times 3$ ), PReLU (initial parameter value is 0.25), 3D batch normalization, dropout (rate is 0.2), 3D Max pooling.

Max pooling kernel size is  $1 \times 2 \times 2$  except for  $3 \times 3 \times 3$  in the last block.

The input channels in convolutional layers are 4 except for 1 in the first block. The output channels are 4.

The number of encoder parameters is 1901.

#### 3.2. Training

The encoder is trained by a triplet comparison as a Siamese neural network. The triplets of samples are selected within a group of experiments. The first two samples in the triplet represent the same class "A". The third sample represents class "B", which is different from "A". The train input is generated as two randomly selected samples taken from the class "A" (can be taken from the same experiment) and one – from the class "B".

The encoder processes the tensors from the train input resulting in three embedding vectors, or embeddings. Two Euclidean distance values are calculated: between the first and second embeddings ("A"- "A" intra-class distance) and between the first and third embeddings ("A"- "B" inter-class distance). The loss of the encoder equals the quotient of inter-class and intra-class distances.

The training parameters: batch size is 20, learning rate is  $2e-3$ , L2 regularization coefficient is 0.1.

Training is divided into two phases: pre-training on synthetic data (optional) and training on real data.

##### 3.2.1. Pre-training phase

Synthetic dataset is used for Pre-training. "A" and "B" classes are selected from two experiments within a group of experiments. Samples are randomly selected from the triplets of Experiments. The number of triplets in the training and validation part is a total of 2400. The number of epochs is 100.

##### 3.2.2. Main training phase

Real dataset is used for the main training phase. The first and second (class "A") Experiments and the third (class "B") Experiment are selected within a group of experiments by the following rules.

- 1) class "A" experiments are either control or with a biomarker;
- 2) if the class "A" experiments are with a biomarker, they have the same odorant;
- 3) class "A" experiments were performed with the same volunteer;
- 4) if both class "A" and "B" experiments with a biomarker, they have different odorants.

As for pre-training phase, random samples are selected from the triplets of experiments. The number of triplets in the training and testing part is a total of 1500. The number of epochs is 25.

#### 3.3. Validation and testing

Validation is used in the pre-training phase, and testing is used in the main training phase.

The pre-training phase uses the synthetic dataset divided into training and validation parts. The validation part contains Groups of experiments different from the training part and was run at the end of each epoch to monitor overfitting.

The main training phase uses the real dataset, divided into training and testing parts. The testing part is an independent part of the dataset (the rat from the test part is not present in the training part). Tests on the testing part were performed after the main training phase.

The tests represent the addition of a fixed algorithm of classification for embeddings calculated by the encoder. The kNN classifier (with  $k = 10$ ) is selected as the classifier.

Two classes are considered: control and with a GC biomarker. We introduce the quartet of experiments (a,b)-(c,d), where a and c are the clear exhalates, while b and d are with the biomarker added. The classifier distinguishes target samples c from d (i.e. the absence of

biomarker from its presence) by matching them with calibration samples a and b. To this end, embeddings are calculated for experiments a, b, c, d; 50 samples were randomly chosen from each experiment. Eight quartets were generated from the testing dataset, covering 1400 samples.

Embeddings calculated for c, d independently were assigned to either control or “with biomarker” classes by the kNN algorithm. Classification results were compared to the ground rules. In this manner, true positive (TP), true negative (TN), false positive (FP), false negative (FN) counts and Accuracy were calculated.

#### 4. Results

The training process consists of two phases: pre-training (on synthetic data) and main training (on real data). Pre-training is optional. Its impact on the method performance was considered, therefore three scenarios were conducted. The first one is without the pre-training phase, where an encoder starts the main training phase having randomized weights. The second scenario starts with the pre-training phase followed by the main training phase. The third scenario is similar to the second scenario, except that learning in the main phase continues only from the same fixed encoder weights obtained after the pre-training phase from the selected encoder trained in the second scenario.

10 independent training sessions were conducted for each scenario resulting in 30 training sessions.

Fig. 1 represents loss on synthetic data (training dataset) averaged by training sessions and its standard deviation during the pre-training. The values of losses after a dramatic drop in the first 20 epochs gradually continue to decrease up to the last 100th epoch. The loss of the encoder selected for the third scenario is mostly within the standard deviation.

The loss values of the real data (training dataset) of the main training phase are illustrated in Fig. 2. On average, both second and third scenarios (with pre-training phase) show lower loss values and their faster decline. However, their standard deviations are approximately two times higher than for the scenario without pre-training.

Given counts of  $TP$ ,  $TN$ ,  $FP$ ,  $FN$ , where positive class corresponds to odor with added cancer biomarker, the following estimations are considered:

$$Accuracy = \frac{TP + TN}{TP + TN + FP + FN};$$

$$Sensitivity = \frac{TP}{TP + FN};$$

$$Specificity = \frac{TN}{TN + FP}.$$

At the end of the main training phase, the estimations are calculated on the real data (testing dataset), the results are presented in Table 2 and in Fig. 3.

Table 2 shows that scenarios with pre-training provide 5–10% higher Accuracy and up to 2–10% higher Sensitivity and Specificity. The scenarios with pre-training demonstrate equal Accuracy, Sensitivity and Specificity values, which means that classifiers recognize positive and negative samples equally well. Scenario of fixed pre-training provides slightly different estimates between the estimates of the first two scenarios. Despite the relatively small increase in average Accuracy when using pre-training, at the end of the section it is shown that a significant difference was achieved.

Fig. 3 illustrates that pre-training scenarios demonstrate higher standard deviation. It is clear that the deviation is a consequence of the presence of sessions with high Accuracy. This is confirmed by the data in Table 3, where 20–40% classifiers trained with the pre-training scenarios provide the Accuracy value above 0.8 and 0.9 thresholds. In contrast, none of the classifiers from the scenario

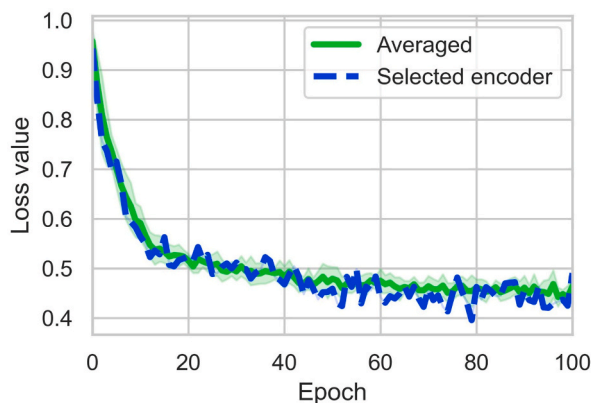
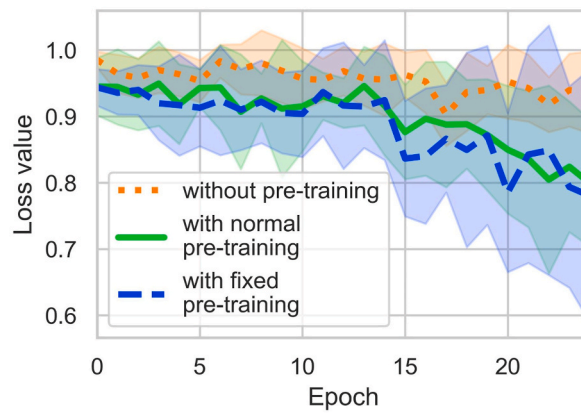


Fig. 1. Averaged train loss value (solid line) with its standard deviation (area around the solid line) during the pre-training phase of the air sample encoder. Dashed line represents loss of the selected encoder. The synthetic dataset used consists of 23,228 training samples.



**Fig. 2.** Averaged train loss value (lines) with its standard deviation (areas around the lines) during the training phase of the air sample encoder. Dotted, solid and dashed lines correspond to scenarios without pre-training, with normal pre-training and with fixed pre-training. The real dataset used consists of 1500 training samples.

**Table 2**

Average values of Accuracy, Sensitivity and Specificity (with their standard deviation) of the classifier of biomarker presence in exhaled air. Data are provided for the last epoch of the training phase. The real dataset used consists of 1500 training and 600 testing samples.

Pre-training scenarios (10 experiment sessions each)	Accuracy	Sensitivity	Specificity
without pre-training	0.68 ± 0.1	0.68 ± 0.1	0.68 ± 0.1
with normal pre-training	0.74 ± 0.2	0.75 ± 0.2	0.74 ± 0.2
with fixed pre-training	0.71 ± 0.2	0.74 ± 0.2	0.69 ± 0.2

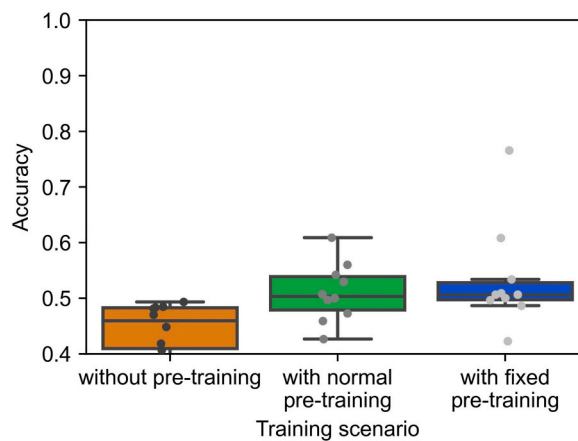


**Fig. 3.** Box plot of Accuracy distribution in the 10 training starts of the classifier of biomarker presence in exhaled breath. The scenarios without pre-training, with normal pre-training and with fixed pre-training are considered. The real dataset used consists of 1500 training and 600 testing samples.

**Table 3**

of trained classifiers of the biomarker presence in exhaled air that achieve the Accuracy thresholds. The scenarios without pre-training, with normal pre-training and with fixed pre-training are considered. The real dataset used consists of 1500 training and 600 testing samples.

Pre-training scenario (10 experiment sessions each)	Accuracy threshold			
	>0.6	>0.7	>0.8	>0.9
without pre-training	80%	50%	0%	0%
with normal pre-training	80%	50%	40%	30%
with fixed pre-training	70%	50%	30%	20%

without pre-training achieved 0.8 Accuracy.

Another estimation of the pre-training impact was done using the Fisher's exact test. By comparing contingency tables (Tables 4 and 5) constructed from counts of sessions Accuracy more than 0.8, we estimate the probability of null-hypothesis (p-value) to be 0.04 for the scenario with pre-training and 0.11 for the fixed pre-training scenario.

## 5. Discussion

The feasibility of recognition of GC biomarker presence in human exhale by bio-hybrid system is evaluated on a short series of experiments. The recognition is based on similarity measured between neural responses in the rat olfactory bulb to different types of odors (clear exhale and exhale + cancer biomarker). The similarity evaluation requires preparation of calibration samples.

The current research is a first step towards developing bio-hybrid approach for cancer screening combining sensory abilities of animals with computer vision and machine learning techniques.

To our knowledge, no reports have been made to apply calcium activity of OB glomeruli into bio-hybrid system. In the past research, microelectrodes and microelectrode arrays were widely used to read information from the olfactory system of mammals for the recognition of volatile compounds [24,25,42,43]. Despite the data on the high efficiency of such systems, it should be noted that the microelectrode method is sensitive to immune responses and electrode movements, which makes it difficult to obtain neural signals for a long period of time [44–46]. In this paper, we take the glomerular calcium activity as a novel sensing element for optical recording. Optical imaging methods are better suited for recording the activity of neurons that project to certain areas [47]. Although calcium imaging has the disadvantage of lower temporal resolution than the microelectrode method, optical imaging is less sensitive to electrical noise and environmental artifacts.

This work presents the results of the feasibility study - the first stage of further comprehensive research. The roadmap of further study includes the following stages.

1. The dependency of cancer biomarker recognition accuracy by a bio-hybrid system on cancer biomarker concentration;
2. The feasibility of cancer biomarkers detection by a bio-hybrid system in exhalates of cancer participants with calibration on artificial cancer biomarkers.

The similarity between evaluation neural responses and calibration neural responses is assessed by a neural model which computes specific spatiotemporal patterns in a response thus transforming a series of calcium dynamics images into encodings representation. Further, the similarity between responses is assessed in encoding space, not in calcium dynamics images space. Since feasibility study involves short series of experiments, we include synthetic samples to pretrain the model. Pre-training aims at enhancing model capabilities to distinguish between different spatiotemporal patterns. We evaluate the pre-training efficiency on synthetic data. Pre-training on synthetic samples in our experiments led to quicker decreasing of loss value during main training phase (on real samples), to higher values of recognition accuracy, and to higher portion of training attempts where high over threshold accuracy (over 0.8) was achieved.

We have the following motivation to involve the pre-training scenario. If we obtain high accuracy of odor classification in this scenario, then we can present a pre-trained encoder as a valuable result of the research. This simplifies its usage in calcium responses classification tasks. If a fixed pre-trained encoder is efficient, then it can be fine-trained on new data and used to encode calcium images into encodings space where classification can be performed by similarity-based methods. If a fixed pre-trained encoder is not efficient comparing to normal pre-training, then we can only propose an architecture of encoder and the whole procedure of pre-training on synthetic data. On our data, although fixed pre-training approach is effective comparing to scenario without pre-training, it doesn't outperform normal pre-training. It possibly means that selection of fixed pre-trained encoder basing on best accuracy on synthetic data is not an optimal strategy. It can be caused by the specifics of real data comparing to simulated data, for example different signal-to-noise ratio, differences in temporal and spatial patterns characteristics of glomeruli activities. We consider it reasonable to focus our further study on the selection of a fixed pre-trained encoder basing on its efficiency on real data and on more realistic modeling of calcium response. The idea of training deep neural networks on big data to obtain visual embeddings [48] (compressed and semantic-containing description of visual representation of objects) is fruitful in different applications of computer vision. Transfer learning approach is based on this idea. It is applied for objects recognition and for images recommendations [49]. Such embeddings are also used to generate visual or text data. Researchers study embeddings disentangling to get particular components or vectors in embeddings space which relate to particular objects or attributes [50]. However, to the best of our knowledge, specific embeddings were not developed for calcium imaging. Computer vision and machine learning efforts related to calcium imaging focus mostly on localization of neurons and extraction of calcium traces [51].

**Table 4**

Contingency table with the number of sessions in which the classifier of biomarker presence in exhaled air achieves the Accuracy threshold of 0.8. The null hypothesis that there is no effect of adding the normal pre-training on achieving the Accuracy threshold has a probability of 0.04.

Pre-training scenario (10 experiment sessions each)	Accuracy >0.8	Accuracy ≤0.8
with normal pre-training	3	7
without pre-training	0	10

**Table 5**

Contingency table with the number of sessions in which the classifier of biomarker presence in exhaled air achieves the Accuracy threshold of 0.8. The null hypothesis that there is no effect of adding the fixed pre-training on achieving the Accuracy threshold has a probability of 0.11.

Pre-training scenario (10 experiment sessions each)	Accuracy >0.8	Accuracy ≤0.8
with fixed pre-training	4	6
without pre-training	0	10

In our work, we present such embeddings obtained on synthetic data. We consider these embeddings together with the method for their computing and general pipeline of bio-hybrid detection of cancer-specific VOCs as the main contribution of our study. Embeddings were derived from calcium images of particular size, duration and frame rate so their application is limited by these constraints. Generalization of such embedding application is the subject to further study. Possible evolution of proposed approach can be based on a large-field-of-view Miniscope for imaging through cranial windows in head-fixed and head-free rats. It would help to make bio-hydrate system portable and simplify screening setup and screening procedure.

We used only male rats due to necessity to take into account the different olfactory sensitivity of female rats at different stages of the estrous cycle. Olfactory activity could fluctuate in females in correlation with the fluctuating levels of sex hormones that are associated with different phases of the estrous cycle. This modulation will present an additional difficulty in the practical use of female animals as part of the bio-hybrid system. Hormonal status of both sexes can influence the initial neural representations of odors, odor detection threshold and odor discrimination [52]. Female mammals generally have a superior sense of smell than males. Female mice have a lower detection threshold, larger spatiotemporal pattern of glomerular activity than in male mice and more rapid olfactory sensory neuron signaling over a broader range of olfactory sensory neurons [53,54]. Broadening of glomerular odor tuning could impair discrimination by increasing overlap in response maps, but conversely the increased number of responding glomeruli in females provides a much richer set of inputs for the brain to interpret [54]. The degree of difference between spatial patterns of glomerular activity predicts the perceptual differences between odors. We cannot exclude the differences between response maps in male and female rats. While we believe gender limitation have not affected the primary outcome of the study, future work could seek to include additional female controls.

Another limitation is the necessity to involve calibration samples to detect cancer biomarkers within our current approach. Our current approach was tested on exhaled breath samples with artificially added cancer biomarkers. Both feasibility of calibration-less biohybrid VOCs detector and its applicability for cancer screening in human are to be further studied.

## 6. Conclusion

Initial research was concluded to validate bio-hybrid approach for the detection of cancer biomarkers in human exhaled air. This approach combines the advantages of rat olfactory sensitivity and capabilities of computer vision and machine learning techniques to detect and recognize biomarker-specific patterns of glomerular activity. Odor evoked calcium response was recorded by a two-photon microscope, encoded, and classified into one of two classes: “clear exhale” and “exhale + cancer biomarker”.

Developed analysis pipeline of rat olfactory responses on cancer biomarkers consists of artificial neural network encoder and kNN classifier. To enhance detection accuracy, simulated dataset was developed which imitates spatiotemporal patterns of rat olfactory responses. Our encoder was pre-trained on this simulated dataset. Classification accuracy reached 0.7 and higher if involves pre-training of encoder on simulated data. We consider pre-trained encoder for calcium imaging analysis together with the method of its pre-training and general pipeline of bio-hybrid approach to detect cancer biomarkers as the main contributions of our work.

## Ethics statement

All animal experimental procedures were approved (Protocol No 4, Date of approval April 28, 2022) in advance by the Ethics Committee of Southern Federal University (Rostov-on-Don, Russia). The human air sampling was approved by the Ethics Committee of Southern Federal University (Protocol No 1, Date of approval May 11, 2018).

## Author contribution statement

Mikhail V. Petrushan; Larisa V. Lysenko: Conceived and designed the experiments; Analyzed and interpreted the data; Contributed reagents, materials, analysis tools or data; Wrote the paper. Aleksey E. Matukhno: Performed the experiments; Contributed reagents, materials, analysis tools or data. Mikhail V. Kopeliovich: Analyzed and interpreted the data; Wrote the paper.

## Funding statement

This work was supported by the Russian Science Foundation № 22–25–00683, <https://rscf.ru/project/22-25-00683/>.

## Data availability statement

The code, data and trained encoders for this project are publicly available and can be accessed via the following link: <https://drive.google.com/drive/folders/1—xo5ecDB-d5-48bezNN5fmZRN77YQp>. For advice on use, please contact the corresponding author.

## Additional information

No additional information is available for this paper.

## Declaration of competing interest

The authors declare that they have no known competing financial interests or personal relationships that could have appeared to influence the work reported in this paper.

## Acknowledgements

The authors express their gratitude to the Advanced Research Foundation for methodological assistance in organizing research and Southern Federal University Strategic Academic Leadership Program (“Priority 2030”) for providing an experimental base for conducting research.

## References

- [1] F. Bray, J. Ferlay, I. Soerjomataram, R.L. Siegel, L.A. Torre, A. Jemal, Global cancer statistics 2018: GLOBOCAN estimates of incidence and mortality worldwide for 36 cancers in 185 countries, *CA A Cancer J. Clin.* 68 (6) (2018) 394–424, <https://doi.org/10.3322/caac.21492>.
- [2] Global Burden of Disease 2019 Cancer Collaboration, J.M. Kocarnik, K. Compton, F.E. Dean, W. Fu, B.L. Gaw, J.D. Harvey, H.J. Henrikson, D. Lu, A. Pennini, R. Xu, E. Ababneh, M. Abbasi-Kangevari, H. Abbastabar, S.M. Abd-El Salam, A. Abdoli, A. Abedi, H. Abidi, H. Abolhassani, I.A. Adedeji, L.M. Force, Cancer incidence, mortality, years of life lost, years lived with disability, and disability-adjusted life years for 29 cancer groups from 2010 to 2019: a systematic analysis for the global burden of disease study 2019, *JAMA Oncol.* 8 (3) (2022) 420–444, <https://doi.org/10.1001/jamaoncol.2021.6987>.
- [3] K.D. Crew, A.I. Neugut, Epidemiology of gastric cancer, *World J. Gastroenterol.* 12 (3) (2006) 354–362, <https://doi.org/10.3748/wjg.v12.i3.354>.
- [4] M.A. Leja, H. Liu, H. Haick, Breath testing: the future for digestive cancer detection, *Expert Rev. Gastroenterol. Hepatol.* 7 (5) (2013) 389–391, <https://doi.org/10.1586/17474124.2013.811033>.
- [5] J. Zhang, Y. Tian, Z. Luo, C. Qian, W. Li, Y. Duan, Breath volatile organic compound analysis: an emerging method for gastric cancer detection, Oct 20, *J. Breath Res.* (4) (2021) 15, <https://doi.org/10.1088/1752-7163/ac2cde>.
- [6] T. Issitt, L. Wiggins, M. Veysey, S.T. Sweeney, W.J. Brackenburg, K. Redeker, Volatile compounds in human breath: critical review and meta-analysis, *J. Breath Res.* (2) (2022 Feb 23) 16, <https://doi.org/10.1088/1752-7163/ac5230>.
- [7] H. Yang, Y. Mou, B. Hu, Diagnostic ability of volatile organic compounds in digestive cancer: a systematic review with meta-analysis. *Clinical medicine insights, Oncology* 16 (2022), 11795549221105027, <https://doi.org/10.1177/11795549221105027>.
- [8] D.N. Bakhmutov, N.N. Kamkin, N.G. Yaryshev, L.B. Lazebnik, Diagnostic Technique for Cancer, RU2538625C1, 2014, 01–20, <https://patents.google.com/patent/RU2538625C1/en#patentCitations>.
- [9] Z.Q. Xu, Y.Y. Broza, R. Ionsecu, U. Tisch, L. Ding, H. Liu, Q. Song, Y.Y. Pan, F.X. Xiong, K.S. Gu, G.P. Sun, Z.D. Chen, M. Leja, H. Haick, A nanomaterial-based breath test for distinguishing gastric cancer from benign gastric conditions, *Br. J. Cancer* 108 (4) (2013) 941–950, <https://doi.org/10.1038/bjc.2013.44>.
- [10] H. Tong, Y. Wang, Y. Li, S. Liu, C. Chi, D. Liu, L. Guo, E. Li, C. Wang, Volatile organic metabolites identify patients with gastric carcinoma, gastric ulcer, or gastritis and control patients, *Cancer Cell Int.* 17 (2017) 108, <https://doi.org/10.1186/s12935-017-0475-x>.
- [11] H. Amal, M. Leja, Y.Y. Broza, U. Tisch, K. Funke, I. Liepniece-Karele, R. Skapars, Z.Q. Xu, H. Liu, H. Haick, Geographical variation in the exhaled volatile organic compounds, *J. Breath Res.* 7 (4) (2013), 047102, <https://doi.org/10.1088/1752-7155/7/4/047102>.
- [12] I. Horváth, Z. Lázár, N. Gyulai, M. Kollai, G. Losonczy, Exhaled biomarkers in lung cancer, *Eur. Respir. J.* 34 (1) (2009) 261–275, <https://doi.org/10.1183/09031936.00142508>.
- [13] S. Dragonieri, V.N. Quaranta, P. Carratu, T. Ranieri, O. Resta, Influence of age and gender on the profile of exhaled volatile organic compounds analyzed by an electronic nose, *J. Bras. Pneumol.* 42 (2016) 143–145, <https://doi.org/10.1590/S1806-3756201500000195>.
- [14] S. Dragonieri, V.N. Quaranta, P. Carratu, T. Ranieri, O. Resta, Exhaled breath profiling by electronic nose enabled discrimination of allergic rhinitis and extrinsic asthma, *Biomarkers* 24 (1) (2019) 70–75, <https://doi.org/10.1080/1354750X.2018.1508307>.
- [15] M.H. Scheepers, Z. Al-Difaie, L. Brandts, A. Peeters, B. van Grinsven, N.D. Bouvy, Diagnostic performance of electronic noses in cancer diagnoses using exhaled breath: a systematic review and meta-analysis, *JAMA Netw. Open* 5 (6) (2022), e2219372–e2219372, <https://doi.org/10.1001/jamanetworkopen.2022.19372>.
- [16] R. Capuano, A. Catini, R. Paolesse, C. Di Natale, Sensors for lung cancer diagnosis, *J. Clin. Med.* 8 (2) (2019) 235, <https://doi.org/10.3390/jcm8020235>.
- [17] C. Hurot, N. Scaramozzino, A. Buhot, Y. Hou, Bio-inspired strategies for improving the selectivity and sensitivity of artificial noses: a review, *Sensors* 20 (6) (2020) 1803, <https://doi.org/10.3390/s20061803>.
- [18] Y. Hirata, H. Oda, T. Osaki, S. Takeuchi, Biohybrid sensor for odor detection, *Lab Chip* 21 (14) (2021) 2643–2657, <https://doi.org/10.1039/d1lc00233c>.
- [19] C. Kim, K.K. Lee, M.S. Kang, et al., Artificial olfactory sensor technology that mimics the olfactory mechanism: a comprehensive review, *Biomater. Res.* 26 (2022) 40, <https://doi.org/10.1186/s40824-022-00287-1>.
- [20] T. Jezierski, M. Walczak, T. Ligor, J. Rudnicka, B. Buszewski, Study of the art: canine olfaction used for cancer detection on the basis of breath odour. Perspectives and limitations, *J. Breath Res.* 9 (2) (2015), 027001, <https://doi.org/10.1088/1752-7155/9/2/027001>.
- [21] E.I. Rodionova, M.Y. Kochevalina, E.V. Kotenkova, V. Morozova, G.A. Kogun, E.L. Bataeva, A.V. Ambaryan, Detection of volatile organic compounds associated with hepatocellular carcinoma by Macrosmatic animals: Approaches to the search for new tumor markers, *Izvestia akademii nauk, Seria Biologicheskaja* (3) (2015) 293–301, <https://doi.org/10.1134/s1062359015030103>.
- [22] G. Lippi, L.M. Heaney, The “olfactory fingerprint”: can diagnostics be improved by combining canine and digital noses? *Clin. Chem. Lab. Med.* 58 (6) (2020) 958–967, <https://doi.org/10.1515/ccml-2019-1269>.
- [23] C. Feil, F. Staib, M.R. Berger, T. Stein, I. Schmidtmann, A. Forster, C.C. Schimanski, Sniffer dogs can identify lung cancer patients from breath and urine samples, *BMC Cancer* 21 (1) (2021) 917, <https://doi.org/10.1186/s12885-021-08651-5>.
- [24] E. Shor, P. Herrero-Vidal, A. Dewan, I. Uguz, V.F. Curto, G.G. Malliaras, C. Savin, T. Bozza, D. Rinberg, Sensitive and robust chemical detection using an olfactory brain-computer interface, *Bioelectron.* 195 (2022), 113664, <https://doi.org/10.1016/j.bio.2021.113664>.
- [25] P. Zhu, S. Liu, Y. Tian, Y. Chen, W. Chen, P. Wang, L. Du, C. Wu, In vivo bioelectronic nose based on a bioengineered rat realizes the detection and classification of multidodorants, *ACS Chem. Neurosci.* 13 (12) (2022) 1727–1737, <https://doi.org/10.1021/acchemneuro.2c00015>.

- [26] C.D. Wilson, G.O. Serrano, A.A. Koulakov, D. Rinberg, A primacy code for odor identity, *Nat. Commun.* 8 (1) (2017) 1477, <https://doi.org/10.1038/s41467-017-01432-4>.
- [27] N. Uchida, Y.K. Takahashi, M. Tanifuji, K. Mori, Odor maps in the mammalian olfactory bulb: domain organization and odorant structural features, *J. Nature Neuroscience* 3 (10) (2000) 1035–1043, <https://doi.org/10.1038/79857>.
- [28] P. Mombaerts, Axonal wiring in the mouse olfactory system, *Annu. Rev. Cell Dev. Biol.* 22 (2006) 713–737, <https://doi.org/10.1146/annurev.cellbio.21.012804.093915>. – doi:.
- [29] Y. Oka, S. Katada, M. Omura, M. Suwa, Y. Yoshihara, K. Touhara, Odorant receptor map in the mouse olfactory bulb: in vivo sensitivity and specificity of receptor-defined glomeruli, *Neuron* 52 (5) (2006) 857–869, <https://doi.org/10.1016/j.neuron.2006.10.019>.
- [30] E.R. Soucy, D.F. Albeanu, A.L. Fantana, V.N. Murthy, M. Meister, Precision and diversity in an odor map on the olfactory bulb, *J. Nature Neuroscience* 12 (2) (2009) 210–220, <https://doi.org/10.1038/nn.2262>.
- [31] A. Gutiérrez-Gálvez, S. Marco, Study of the coding efficiency of populations of olfactory receptor neurons and olfactory glomeruli, in: K.C. Persaud, S. Marco, A. Gutiérrez-Gálvez (Eds.), *Neuromorphic Olfaction*, CRC Press/Taylor & Francis, Boca Raton (FL), 2013.
- [32] S.D. Burton, A. Brown, T.P. Eiting, I.A. Youngstrom, T.C. Rust, M. Schmuker, M. Wachowiak, Mapping odorant sensitivities reveals a sparse but structured representation of olfactory chemical space by sensory input to the mouse olfactory bulb, *Elife* 11 (2022), e80470, <https://doi.org/10.7554/eLife.80470>.
- [33] S. Sankaran, L.R. Khot, S. Panigrahi, *Biology and applications of olfactory sensing system: a review*, *Sensor. Actuator. B Chem.* 171 (2012) 1–17.
- [34] K.E. Schackart III, J.Y. Yoon, Machine learning enhances the performance of bio-receptor-free biosensors, *Sensors* 21 (16) (2021) 5519.
- [35] J. Lu, J. Hu, J. Zhou, Deep metric learning for visual understanding: an overview of recent advances, *IEEE Signal Process. Mag.* 34 (6) (2017) 76–84, <https://doi.org/10.1109/MSP.2017.2732900>.
- [36] Y. Saalberg, H. Bruhns, M. Wolff, Photoacoustic spectroscopy for the determination of lung cancer biomarkers—A preliminary investigation, *Sensors* 17 (1) (2017) 210, <https://doi.org/10.3390/s17010210>.
- [37] R.A. Arefev, V.N. Kirov, N.V. Bulat, M.V. Petrushan, M.O. Burebelov, S.L. Sazhin, B.M. Vladimirovskiy, A.E. Matukhno, V.V. Chechevatova, V.G. Semykina, L. V. Lysenko, Methods for calculating the stereotaxic coordinates of rat brain structures by pixel coordinates of the image obtained by confocal and two-photon laser scanning microscopy, *J. Neurosci. Methods* 361 (2021), 109273, <https://doi.org/10.1016/j.jneumeth.2021.109273>.
- [38] A. Vinograd, Y. Livneh, A. Mizrahi, History-dependent odor processing in the mouse olfactory bulb, *J. Neurosci.* : the official journal of the Society for Neuroscience 37 (49) (2017) 12018–12030, <https://doi.org/10.1523/JNEUROSCI.0755-17.2017>.
- [39] Y. Adam, Y. Livneh, K. Miyamichi, M. Groyzman, L. Luo, A. Mizrahi, Functional transformations of odor inputs in the mouse olfactory bulb, *Front. Neural Circ.* 8 (2014) 129, <https://doi.org/10.3389/fncir.2014.00129>.
- [40] C. Tischbirek, A. Birkner, H. Jia, B. Sakmann, A. Konnerth, Deep two-photon brain imaging with a red-shifted fluorometric Ca<sup>2+</sup> indicator, *Proc. Natl. Acad. Sci. U.S.A.* 112 (36) (2015) 11377–11382, <https://doi.org/10.1073/pnas.1514209112>.
- [41] C.H. Tischbirek, T. Noda, M. Tohmi, A. Birkner, I. Nelken, A. Konnerth, In vivo functional mapping of a cortical column at single-neuron resolution, *Cell Rep.* 27 (5) (2019) 1319–1326.e5, <https://doi.org/10.1016/j.celrep.2019.04.007>.
- [42] L. Zhuang, T. Guo, D. Cao, L. Ling, K. Su, N. Hu, P. Wang, Detection and classification of natural odors with an in vivo bioelectronic nose, *Biosens. Bioelectron.* 67 (2015) 694–699, <https://doi.org/10.1016/j.bios.2014.09.102>.
- [43] K. Gao, S. Li, L. Zhuang, S. Qin, B. Zhang, L. Huang, P. Wang, In vivo bioelectronic nose using transgenic mice for specific odor detection, *Biosens. Bioelectron.* 102 (2018) 150–156, <https://doi.org/10.1016/j.bios.2017.08.055>.
- [44] R. Biran, D.C. Martin, P.A. Tresco, The brain tissue response to implanted silicon microelectrode arrays is increased when the device is tethered to the skull, *J. Biomed. Mater. Res.* 82 (1) (2007) 169–178, <https://doi.org/10.1002/jbm.a.31138>.
- [45] J. Thelin, H. Jörmteell, E. Psouni, M. Garwicz, J. Schouenborg, N. Danielsen, C.E. Linsmeier, Implant size and fixation mode strongly influence tissue reactions in the CNS, *PLoS One* 6 (1) (2011), e16267, <https://doi.org/10.1371/journal.pone.0016267>.
- [46] L.S. Kumosa, Commonly overlooked factors in biocompatibility studies of neural implants, *Adv. Sci.* 10 (6) (2023), e2205095, <https://doi.org/10.1002/adv.202205095>.
- [47] G.J. Broussard, L. Petreanu, Eavesdropping wires: recording activity in axons using genetically encoded calcium indicators, *J. Neurosci. Methods* 360 (2021), 109251, <https://doi.org/10.1016/j.jneumeth.2021.109251>.
- [48] A. Frome, G.S. Corrado, J. Shlens, S. Bengio, J. Dean, Mikolov T. Ranzato Ma, DeViSE: a deep visual-semantic embedding model, in: C.J. Burges, L. Bottou, M. Welling, Z. Ghahramani, K.Q. Weinberger (Eds.), *Advances in Neural Information Processing Systems*, 26, Curran Associates, Inc, 2013, in: <https://proceedings.neurips.cc/paper/2013/file/7cce53cf90577442771720a370c3c723-Paper.pdf>.
- [49] F. del-Río, P. Messina, V. Dominguez, D. Parra, Do Better ImageNet Models Transfer Better for Image Recommendation? *ArXiv*, 2018, 09870 abs/1807.
- [50] N. Saini, K. Pham, A. Shrivastava, Disentangling Visual Embeddings for Attributes and Objects, *2022 IEEE/CVF Conference on Computer Vision and Pattern Recognition (CVPR)*, 2022, pp. 13648–13657.
- [51] Z. Dong, W. Mau, Y. Feng, Z.T. Pennington, L. Chen, Y. Zaki, K. Rajan, T. Shuman, D. Aharoni, D.J. Cai, Minian, an open-source miniscope analysis pipeline, *Elife* 11 (2022), e70661, <https://doi.org/10.7554/eLife.70661>.
- [52] T. Abaffy, H.Y. Lu, H. Matsunami, Sex steroid hormone synthesis, metabolism, and the effects on the mammalian olfactory system, *Cell Tissue Res.* 391 (1) (2023) 19–42, <https://doi.org/10.1007/s00441-022-03707-9>.
- [53] M.J. Baum, E.B. Keverne, Sex difference in attraction thresholds for volatile odors from male and estrous female mouse urine, *Horm. Behav.* 41 (2) (2002) 213–219, <https://doi.org/10.1006/hbeh.2001.1749>.
- [54] M.D. Kass, L.A. Czarnecki, A.H. Moberly, J.P. McGann, Differences in peripheral sensory input to the olfactory bulb between male and female mice, *Sci. Rep.* 7 (2017), 45851, <https://doi.org/10.1038/srep45851>.